JOURNAL OF THERMOPHYSICS AND HEAT TRANSFER
Vol. 22, No. 3, July–September 2008

Erratum

Spectroscopic Analysis of Titan Atmospheric Plasmas

M. Playez* and D. G. Fletcher†
Von Kármán Institute for Fluid Dynamics, 1640 Rhode Saint Genèse, Belgium

DOI: 10.2514/1.38894

The figures in this paper, published in the April–June issue of the *Journal of Thermoplastics and Heat Transfer*, were printed in black and white instead of color in the print version of the journal. The entire article is reproduced below with the figures in color as the author intended. AIAA regrets the error.

The analysis of emission spectroscopy measurements performed on plasmas with a composition representative of the atmosphere of Titan is presented. The plasmas are produced in the von Kármán Institute for Fluid Dynamics Minitorch inductively coupled plasma wind tunnel. Absolute volume emissivities are obtained for two different test conditions. The first one, a high-pressure test condition, is selected to obtain conditions close to local thermodynamic equilibrium. The second one, a low-pressure test condition, is selected to investigate possible departure from equilibrium conditions. The analysis of the measured spectra is performed with a radiation code developed at the von Kármán Institute for Fluid Dynamics for this purpose. Dynamic behavior of the plasma jet is considered and the effect of observed fluctuations is included in the analysis. An estimated radial distribution of the error induced by the fluctuations on the measured volume emissivity is computed. Good agreement between measurement and computation is obtained for the high-pressure test condition at the center of the jet. For larger radial positions the error induced by the fluctuations increases and greater corrections have to be applied. A preliminary analysis of the low-pressure test condition at the center of the jet leads to the introduction of large overpopulation factors attributed to the emitting vibrational and electronic energy levels.

I. Introduction

EVEN if performed at moderate speed (6–10 km/s) [1–7], entry or aerocapture maneuvers in the atmosphere of Titan are characterized by significant radiation emission in the shock layer surrounding the space probe. This strong emission is due to the composition of the atmosphere of Titan, which is mainly composed of nitrogen with a small percentage of methane. When this mixture is brought to high temperature, strong radiators, CN and C_2 molecules, are produced. In such conditions, the energy released in the form of radiation comprises an important fraction of the heat flux impinging on the heat shield. An accurate estimate of this radiative heat flux is therefore necessary for a proper design of the thermal protection system. Moreover, the radiation emission is strongly dependent on the nonequilibrium conditions present behind the shock wave, which requires implementation of collisional-radiative models for accurate prediction of the emitted radiation. Such models are under development for the prediction of the nonequilibrium population distribution in Titan atmosphere plasmas [8,9]. Nevertheless, no electronically and vibrationally resolved collisional-radiative models are currently available. Because the development and testing of such models requires experimental data, the present paper summarizes a study aimed at providing such data.

Inductively coupled plasma (ICP) wind tunnels are used in the aerospace field for the replication of the high-temperature boundary layer on the stagnation line of space vehicles, provided that the conditions at the outer edge of the boundary layer and at the wall are the same in flight and in the wind tunnel [10]. These facilities do not offer the possibility to fully simulate the relaxation processes present behind a shock wave, because the plasma production mechanism is different. Nevertheless, ICP wind tunnels have demonstrated their use in the validation of plasma emission computation under local thermodynamic equilibrium (LTE) conditions [11] and can provide nonequilibrium conditions for the analysis of collisional energy transfer processes [12]. Emission spectroscopy measurements performed in the VKI Minitorch ICP facility are presented in this paper [13]. The test campaign can be divided in two steps. The first step is the production and analysis of spectra emitted under LTE conditions. This analysis provides a reference for the validation of both experimental procedures and spectral modeling. The second step is the measurement of nonequilibrium spectra, producing data for the development of electronically and vibrationally resolved collisional-radiative models. As stated earlier, the nonequilibrium flow conditions in the immediate postshock region present during entry or aerocapture in the atmosphere of Titan, which have been computed for flight conditions [1–9] or simulated in shock tubes [14–17], cannot be replicated in the facility used for the present investigation. Moreover, the total specific enthalpy of the VKI Minitorch facility, which was in the range of 8–10 MJ/kg on the jet axis, is rather low with respect to the required values ranging from 12.5 to 15 MJ/kg for peak radiative heating of the Huygens entry [9]. Other ICP wind-tunnel facilities, such as the VKI Plasmatron, can provide higher specific enthalpy values (theoretically, up to 75-MJ/kg mass-averaged total specific enthalpy) and its use could be considered for future development. However, the VKI Minitorch facility was selected in this study because it can produce the high-pressure plasma flows required to achieve LTE conditions, and its long-duration operation allows detailed analysis of the plasma state.

After presentation of the VKI Minitorch facility and a description of the dynamic behavior of the plasma jet, the emission spectroscopy setup is described. The results of this study are then presented: The spectral radiation model developed at VKI for the analysis of the test conditions is described and the spectra obtained for the two different conditions described previously are analyzed.

Received 2 June 2008; accepted for publication 2 June 2008.

*Senior Research Engineer, Aerospace and Aeronautics Department. Member AIAA.

†Professor, Head of Aerospace and Aeronautics Department. Associate Fellow AIAA.

II. Facility

The tests were performed in the VKI Minitorch, which is an ICP wind tunnel. Its working principle is illustrated in Fig. 1. The test gas is injected through a gap between the inner block and the quartz tube. A high-radio-frequency (27-MHz) current is applied to the coil and induction heating takes place inside the quartz tube, producing a plasma. At this location, the plasma is known to be in nonequilibrium conditions [18]. It relaxes and cools while flowing toward the measurement location. If the relaxation processes are sufficiently fast, LTE conditions can be produced at the measurement location, about 6 cm above the last coil turn. The plasma exits the quartz tube to enter a vacuum chamber in which the chamber pressure is varied to change the test conditions.

The different parameters defining the VKI Minitorch are given in Table 1. The indicated pressure range corresponds to the static pressure inside the test chamber, which for the subsonic plasma flow corresponds very nearly to the total pressure. A pressure tap placed on the wall of the test chamber monitors the static pressure of the plasma flow. The pressure inside the test chamber is varied by adjusting a variable aperture valve placed on the vacuum line. Two test conditions were selected: a high-pressure test condition, with a pressure equal to 300 mbar, and a low-pressure test condition, with a pressure equal to 23 mbar. The pressure in the chamber was limited to 300 mbar for the present study because further increase of the test chamber pressure leads to lower emission of the plasma jet and higher stray light produced in the induction region. The second test condition offered the lowest static pressure available and therefore

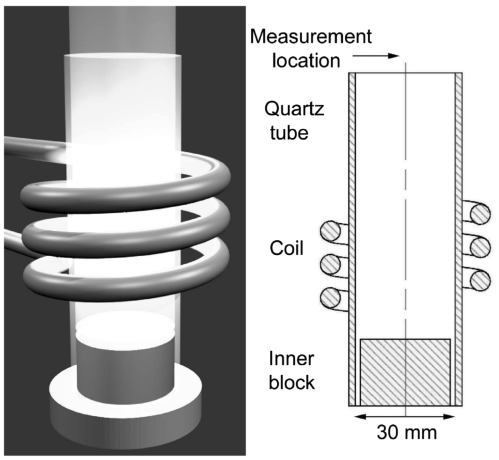

Fig. 1 Working principle of the VKI Minitorch plasma wind tunnel.

Table 1 VKI Minitorch working parameters

Power (in the plasma)	3.75 kW
Frequency	27 MHz
Mixture components	N_2, CH_4
Mass flow	0.6 g/s
Quartz tube inner diameter	30 mm
Vacuum chamber inner diameter	300 mm
Pressure range	20 mbar to 1 bar

less efficient relaxation mechanisms. The test gas composition used in the present study is 98.1% nitrogen and 1.9% methane by volume.

The emission spectroscopy measurements presented in this paper were implemented assuming the plasma jet was steady. However, it appeared in the course of this study that the plasma jet of the VKI Minitorch beats periodically. High-speed imaging of the plasma jet was performed to analyze and to eventually reduce the strength of these fluctuations. A Phantom v7.0 high-speed camera was used for this purpose, with acquisition frequencies up to 100 kHz. Small changes in the geometry of the plasma torch led to a significant reduction in the plasma emission fluctuations. In the nominal geometric configuration of the torch, at the center of the jet, the plasma emission decreases to 20% of its maximum value. After correction of the torch geometry, the minimum plasma emission is 80% of the maximum emission at the same radial and axial location. The plasma fluctuations measured in the final configuration are illustrated in Fig. 2, in which the plasma emission at the center of the jet is plotted for different pressures. Two types of fluctuations are superimposed. The first is linked to the variation with time of the envelope of the RF power coupled to the plasma. It occurs with a frequency equal to 300 Hz and is due to the imperfect rectification of the current feeding the electric valve of the RF generator. The second type of fluctuation is linked to the occurrence of vortex shedding from the recirculation bubble present behind the inner block of the injection system. In the present design of the torch, this recirculation bubble is used to stabilize the plasma ball. This second type of fluctuation is frequency-locked to the power fluctuations.

Following modifications to the injector and torch, the variation of the emission radial profile in the final configuration is illustrated in Fig. 3 for the 300-mbar test condition. The solid lines represent the emission profile on one side of the plasma jet (from the center of the jet to the outside of the jet) and the dashed lines show the behavior of the other side of the jet. The superposition of the two curves indicates a good symmetry of the plasma flow. The time label printed on each plot indicates the time delay between the acquisition of the picture and the beginning of the sequence. The amplitude of the emission fluctuations is small at the center of the jet: close to 10%. Larger

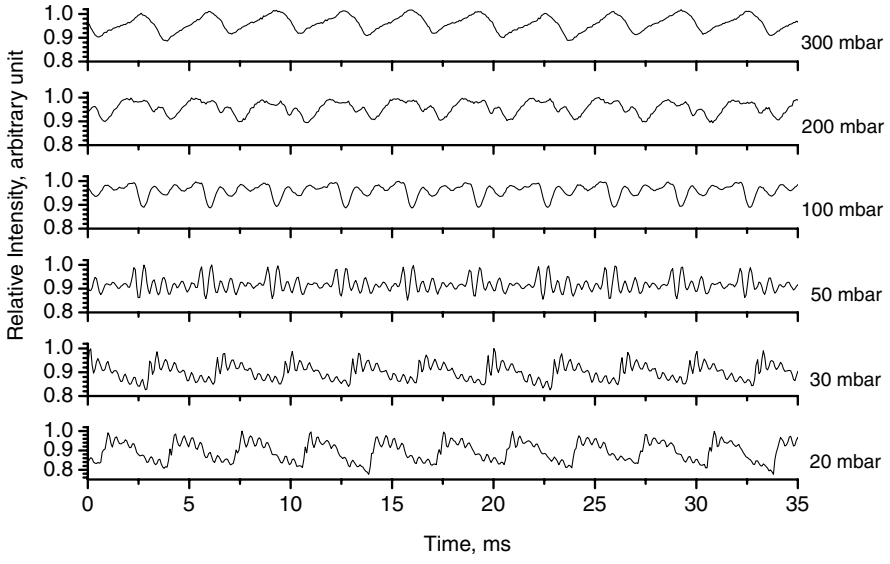

Fig. 2 Measurement of the plasma emission fluctuations at the center of the jet.

variations occur at the edge of the plasma, where large gradients are present. In the low-pressure test condition, the emission fluctuations at the center of the jet are equal to 22% of the maximum emission value (see Fig. 2).

The temporal evolution of the emission profiles presented in Fig. 3 are used for the evaluation of the effect of the fluctuations on the volume emissivity obtained after Abel inversion in the emission spectroscopy experiment. The intensity values obtained with the high-speed camera correspond to the spectral emission of the plasma integrated over the spectral response range of the camera. The different spectral features composing the emission spectra have different temperature dependencies and therefore different radial intensity distributions and different temporal variations. These radial distributions and temporal variations are also different from the distributions and variations of the spectrally integrated value. This procedure thus only gives an indication of the effect of the fluctuations on the different spectral features observed in the spectra. The Abel inversion is applied to the emission profiles plotted in Fig. 3 for each picture of the high-speed movie. The average inverted profile and the corresponding maximum and minimum are given in Fig. 4. The relative errors computed from the differences between the envelop and the averaged profile of Fig. 4 are plotted in Fig. 5. Close to the center of the jet, the effect of the fluctuations is limited to errors lower than 8%, whereas in the region of large emission gradients, larger errors are induced, increasing up to 60% for radial positions at which the plasma emission remains measurable.

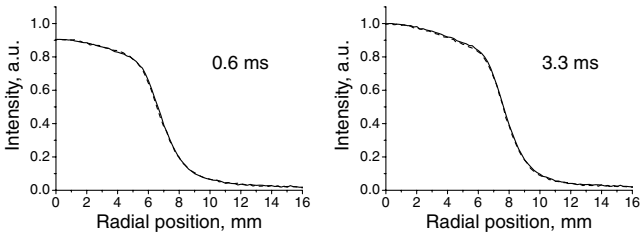

Fig. 3 Temporal evolution of the emission profile at 300 mbar, optimized geometrical configuration.

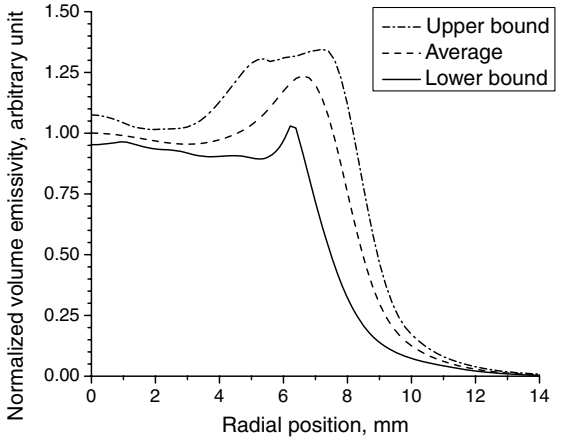

Fig. 4 Envelope and average value of the Abel-inverted emission fluctuations at $P = 300$ mbar, optimized geometry.

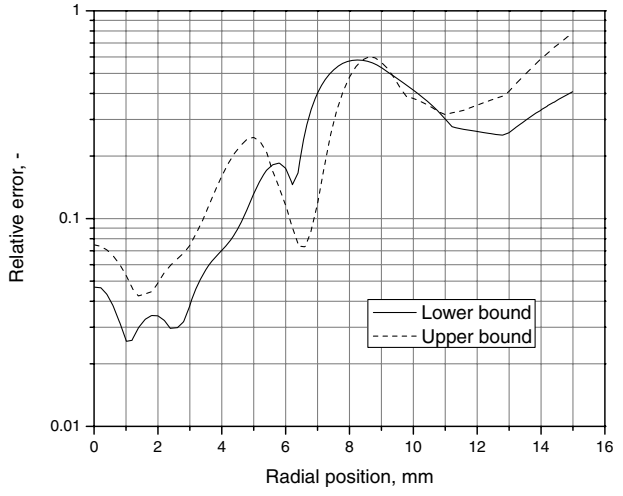

Fig. 5 Estimation of the relative uncertainty of the measured volume emissivity due to the plasma fluctuations at $P = 300$ mbar.

III. Instrumentation

The plasma emission collection system implemented for the present measurement is shown in Fig. 6. The light is collected by a 50-mm-diam, 300-mm-focal-length spherical mirror. After a second reflection on a flat mirror, the light enters an optical fiber. Both mirrors are UV-enhanced aluminum mirrors. The use of mirrors makes the system achromatic. To increase the f-number of the system, a variable diameter aperture is added between the flat mirror and the optical fiber entrance. The aperture also reduces the amount of stray light entering the fiber. The f-number of the system is set to at least 26, making the collection volume very close to a cylinder over the whole plasma diameter. This is a necessary condition for the application of the Abel inversion. The measurements were calibrated using an Osram WI17G tungsten ribbon lamp. The implemented calibration procedure limits the investigation to the spectral range of 350–1000 nm. The light emitted by the plasma was analyzed using an Ocean Optics HR2000CG-UV-IR spectrometer. The characteristics of this spectrometer are given in Table 2. The full-width half-maximum of the apparatus function was measured observing light diffracted from a He-Ne laser beam and is equal to 1.1 nm.

IV. Results

A. Spectra Modeling

To determine the state of the plasma from the measured volume emissivity spectra, modeling of the plasma emission is required. A radiation code dedicated to the modeling of the emission of plasmas representative of Titan atmosphere was implemented for this purpose. The spectra are modeled in the 350–1000-nm wavelength range. The emission of the molecules CN, C_2, and N_2 is taken into account. The emission of the atomic lines of H, C, and N was also included in the computations but their contribution was found to be negligible. Three systems of the CN molecule are modeled: the CN violet [19–21] ($B^2\Sigma^+ \rightarrow X^2\Sigma^+$), CN red [20,22,23] ($A^2\Pi \rightarrow X^2\Sigma^+$) and CN leblanc [19,20,22] ($B^2\Sigma^+ \rightarrow A^2\Pi$). The C_2 Swan [21,24–26] ($d^3\Pi_g \rightarrow a^3\Pi_u$), C_2 Phillips [27,28] ($A^1\Pi_u \rightarrow X^1\Sigma_g^+$), and C_2 Deslandres-D'Azambuja [27–29] ($C^1\Pi_g \rightarrow A^1\Pi_u$) systems were considered, as well as the N_2 first positive [11,30,31] and second positive [11,32] systems ($B^3\Pi_g \rightarrow A^3\Sigma_u^+$ and $C^3\Pi_u \rightarrow B^3\Pi_g$). However, only the CN systems and the C_2 Swan system have nonnegligible contributions for our test conditions.

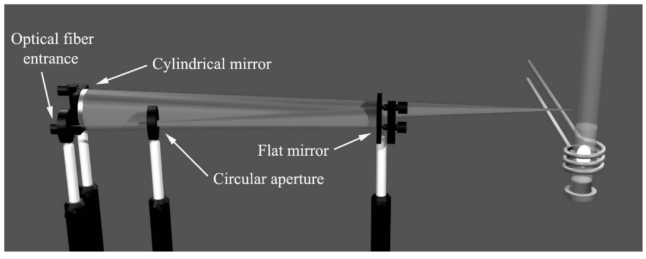

Fig. 6 Emission spectroscopy setup schematic: plasma emission collection optics.

Table 2 Characteristics of the Ocean Optics HR2000-UV-IR spectrometer

Wavelength range	200–1100 nm
Grating	300 grooves/mm
f-number	4
Entrance slit width	5 μm
Detector	2048-element linear silicon CCD array

B. Comparison of Measurement and Modeling

After Abel inversion of the measured absolute intensity profiles, the measured absolute volume emissivity values are compared with the modeled emission. The analysis of the high-pressure test condition is performed as follows. In the wavelength range of 430–900 nm, the relative spectral distribution of the volume emissivity is fitted with a synthetic spectrum computed under the assumption of LTE conditions. A temperature is then obtained. In this wavelength range, spectral features of the three main systems, CN violet ($\Delta v = -2$), CN red (Δv ranging from $+2$ to $+6$), and C_2 Swan (mainly $\Delta v = -1, 0,$ and $+1$) are present. As a working hypothesis, the radiation self-absorption is supposed to be negligible and is not taken into account in the Abel inversion. The validity of this hypothesis is discussed in a following paragraph. The temperature obtained from the fitting procedure is based on the comparison of the spectral distribution of the different systems: on the relative strength of the bands and on the distribution in the bands, but also on the relative strength of the different systems of CN and on the relative strength of the systems of two different species, CN and C_2. This procedure therefore brings information on the chemical composition of the plasma, as well as on the electronic, vibrational, and rotational distributions of the energy levels. If a good agreement between the LTE computation and the measurements is obtained, the distribution among the different energy levels responsible for the emission and the plasma composition can be considered to be close to their equilibrium values.

Following the temperature determination, the measurements are compared with the computations on an absolute scale. To account for possible bias present in the computations and measurements, a correction factor is introduced. It multiplies the computed spectra over the whole spectral range of interest. A correction factor equal to unity would naturally correspond to excellent agreement between computation and measurement. Among the different biases possibly present in the computations and measurements, the correction factor accounts for the effect of the plasma fluctuations on the measurement. This correction is important for radial positions at which large fluctuations are present.

The comparison between computations and measurements is repeated for each measurement location on the radial profile of the jet. The temperature and correction factor distributions plotted in Figs. 7 and 8 are then obtained. For radial positions greater than 9 mm, the quality of the fit deteriorates, owing to the weaker emission intensity, and a linear extrapolation of the temperature profile is preferred to the computed temperature values. The quality of the fit between measurement and model are shown in Figs. 9–11 for three different temperature values ranging from 3600 to 5000 K. The correction factor is given in the label of the computed spectra.

The uncertainty analysis of the measurements and computations was performed as follows: 5% accuracy was attributed to the calibration of the system and 8% was attributed to the unresolved fluctuations of emission. At the center of the jet, 8% uncertainty was attributed to the Abel inversion. Therefore, for this radial position, a 21% estimated error is obtained for the measurements. Concerning the computations, 5% accuracy is attributed to the transition probabilities of CN [20] and 5% to the equilibrium composition computation [13], leading to a total accuracy of 10%. Those estimates can reasonably account for the observed discrepancy. At the center of the jet, the scaling factor equals 0.72, which corresponds to a 28% error. The decrease of the correction factor when the radial position increases can be correlated to the increase of the error induced by the plasma fluctuations.

The assumption of an optically thin plasma (i.e., without absorption of the emitted light by the plasma itself), was made in the previous analysis. To check this assumption, the intensity spectrum measured at the center of the jet is reconstructed from the temperature and correction factor profiles of Figs. 7 and 8. This computation is performed with and without taking into account the plasma absorption. The spectral distribution of the difference of the two

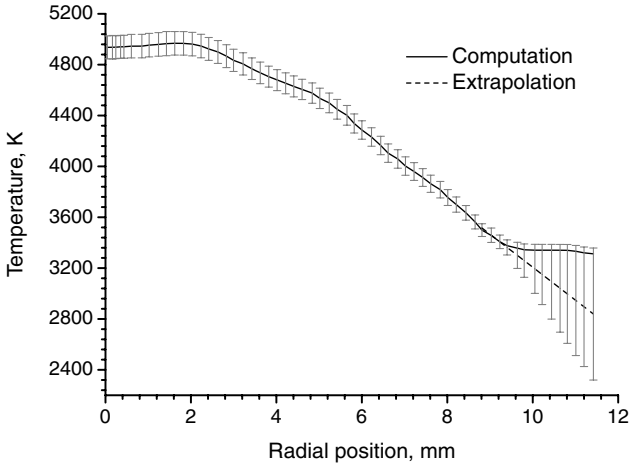

Fig. 7 Computed temperature profile, $P = 300$ mbar.

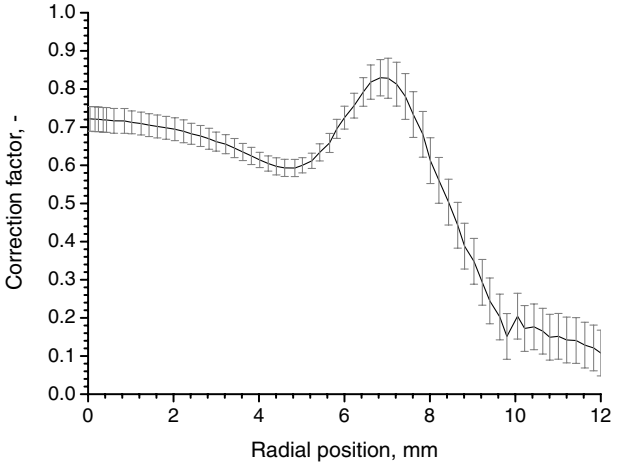

Fig. 8 Computed correction factor profile; $P = 300$ mbar.

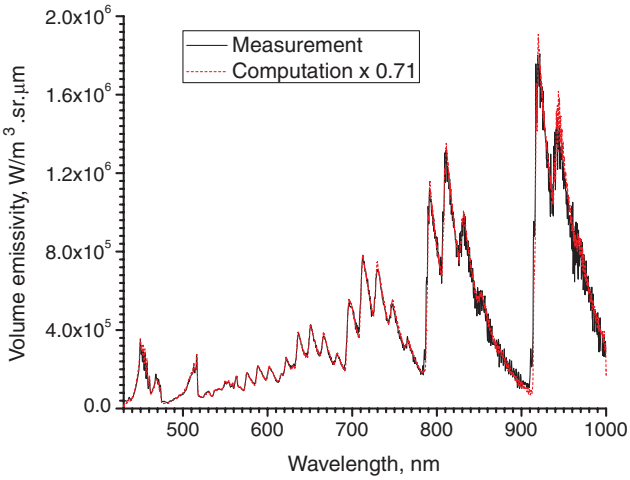

Fig. 9 Comparison of the measured and computed volume emissivities between 430 and 1000 nm; $r = 1.24$ mm; $T = 4959$ K and $P = 300$ mbar.

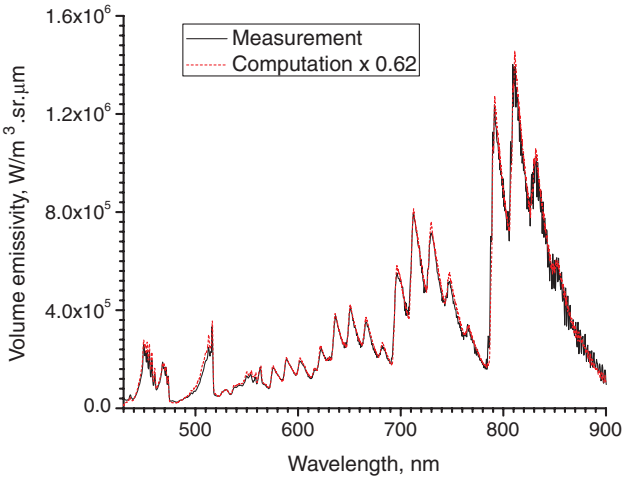

Fig. 10 Comparison of the measured and computed volume emissivities between 430 and 900 nm; $r = 3.82$ mm; $T = 4706$ K and $P = 300$ mbar.

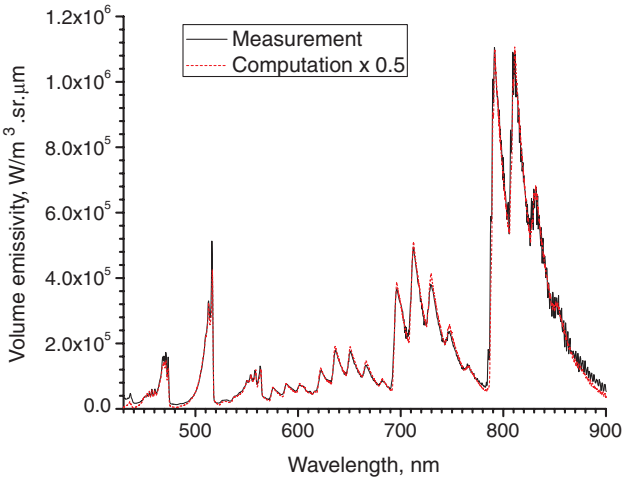

Fig. 11 Comparison of the measured and computed volume emissivities between 430 and 900 nm; $r = 8.43$ mm; $T = 3634$ K and $P = 300$ mbar.

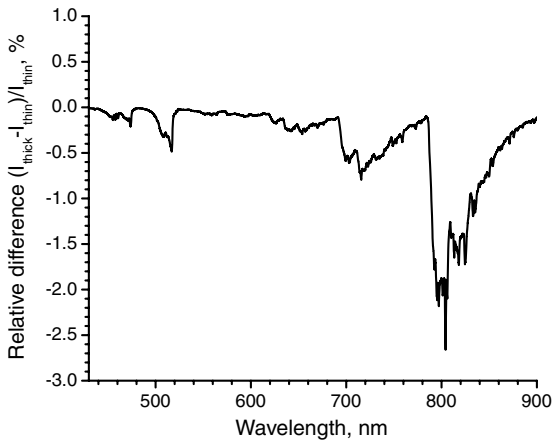

Fig. 12 Computed difference between optically thin and optically thick plasma conditions at the center of the jet; 430–900-nm interval; $P = 300$ mbar.

computations is shown in Fig. 12. The maximum relative difference between the two spectra is less than 2.7% over the spectral interval of interest. This difference is negligibly small, thereby validating the assumption of an optically thin plasma. The same computation was

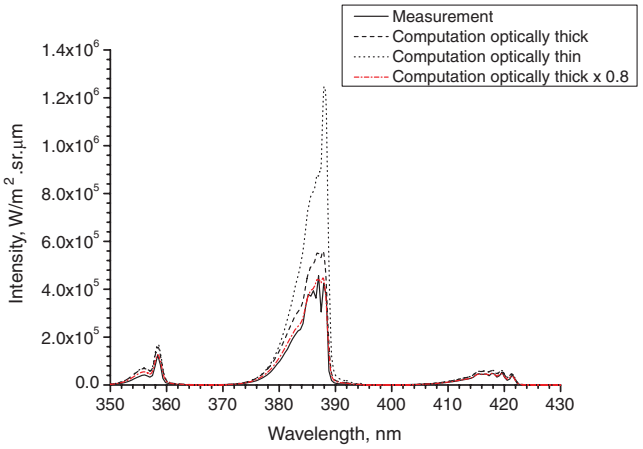

Fig. 13 Computed intensity at the center of the jet; 350–430-nm interval; $P = 300$ mbar.

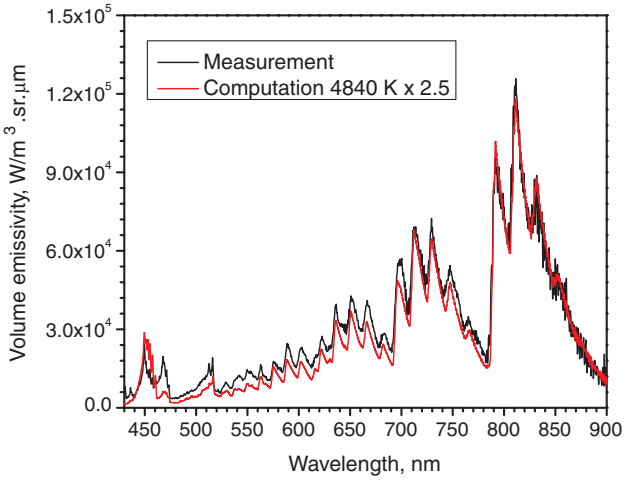

Fig. 14 LTE computation analysis of the 23-mbar case; comparison of the LTE computation and the measured spectrum.

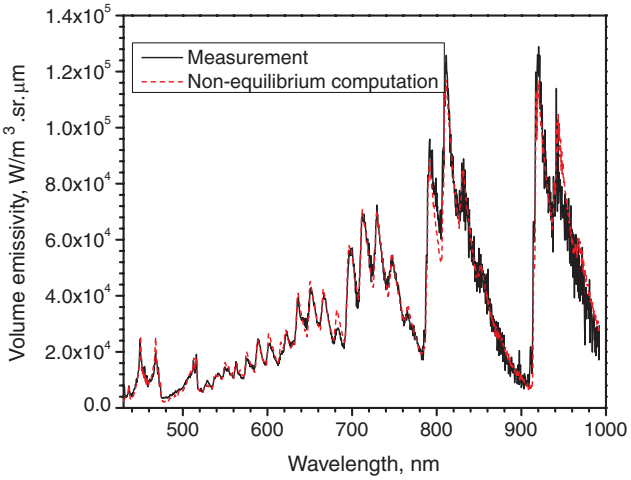

Fig. 15 Comparison of the measured and computed spectrum after introduction of the overpopulation factors; $T = 4840$ K and $P = 23$ mbar.

performed for the wavelength range of 350–430 nm. The result of this computation is presented in Fig. 13. Strong absorption of the CN violet main band ($\Delta v = 0$) is obtained, the optically thick computation giving a peak intensity close to two times smaller than the optically thin computation. Nevertheless, a 20% difference between the optically thick computation and the measured spectrum

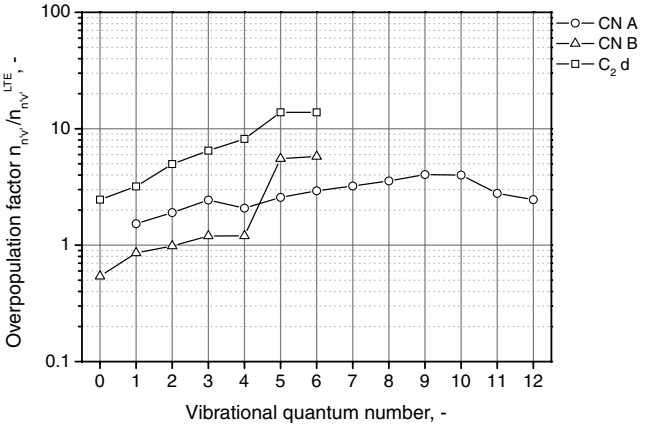

Fig. 16 Computed overpopulation factors; $T = 4840$ K and $P = 23$ mbar.

is present. The origin of this discrepancy is not clearly identified; however, it is of the same order of magnitude as the correction for plasma intensity fluctuations. A nonequilibrium population distribution of the strongly emitting CN B electronic state could also produce such a result, but this is considered less likely in view of the good agreement with LTE conditions for the other band systems. Temporally resolved measurements or modification of the torch design to suppress the plasma fluctuations should therefore be performed before drawing conclusions on the observed differences.

A preliminary analysis of the spectra obtained at 23 mbar, following the procedure described next, leads to large deviations between the computed and measured spectrum (see Fig. 14). Overpopulation factors are therefore introduced in the analysis. They are given as the ratio of the actual number density of the emitting vibronic level $n'v'$ and its density under LTE conditions. The overpopulation factors can only be estimated for the low-lying vibrational levels of the electronic states, CN B, CN A, and C_2 d. Figure 15 shows the result of the modified procedure. The comparison is performed for only one radial position, at the center of the jet, where the plasma fluctuations have the least influence. The measured temperature is equal to 4840 K and corresponds to the rotational temperature of the flow. The obtained overpopulation factors are plotted in Fig. 16. Because of the low spectral resolution used in the present study, the bands associated with CN B $v' = 5$ and 6 overlap and the determined overpopulation factors are strongly correlated. The same problem arises for the C_2 d $v' = 5$ and 6 overpopulation factors and the same value is used for the two factors. The overpopulation factor distributions show large deviations from unity. Only the C_2 d electronic state shows a regular increase in the population of its vibrational levels. The CN A v' states can be divided into three distributions. The first two, for v' ranging from 1 to 3 and 4 to 9, show a regular increase of the overpopulation factor with the vibrational quantum number, whereas the higher vibrational levels show an opposite trend. The low vibrational states ($v' = 1$ and 2) of the CN B state are underpopulated, whereas the higher vibrational levels ($v' = 2$–4) are close to unity. The CN B $v' = 5$ and 6 states exhibit high overpopulation factors. Nevertheless, the results of this measurement have to be taken with care because the possible effects of the plasma fluctuations on the overpopulation factors have not been considered.

V. Conclusions

A spectroscopic analysis of the emission of plasmas with a composition representative of the atmosphere of Titan is described in this paper. An investigation of the dynamic behavior of the plasma jet was conducted. Periodic fluctuations of the plasma jet were observed. These fluctuations have two origins: the RF-induced power fluctuations and vortex shedding from the plasma ball. The fluctuations could not be completely suppressed, but small changes in the torch geometry led to a significant decrease of the observed plasma jet fluctuations. The effect of these fluctuations on the time-averaged emission spectroscopy measurements was considered. An estimate of the induced error is obtained and included in the analysis of the emission spectroscopy measurements. At high pressure (300 mbar), in the center of the jet, a good match is obtained between the measured volume emissivity spectra and the corresponding LTE computation, thereby justifying the implementation of the measurements and computations. For higher radial positions, the effect of the plasma fluctuations increases, leading to larger differences on the absolute volume emissivity scale. The analysis of measurements performed at low pressure (23 mbar) showed large deviations from the emission under LTE conditions. Overpopulation factors are extracted for three electronic states, CN B, CN A, and C_2 d. Equilibrium and nonequilibrium test conditions were thus obtained and analyzed. The implemented procedure offers the possibility to obtain data for the development of electronically and vibrationally resolved collisional-radiative models. Further developments of the setup should either resolve the plasma fluctuations or fully suppress them.

References

[1] Takashima, N., Hollis, B., Zoby, E., Sutton, K., Olejniczak, J., Wright, M., and Prabhu, D., "Preliminary Aerothermodynamics Analysis of Titan Aerocapture Aeroshell," AIAA Paper 2003-4952, July 2003.

[2] Olejniczak, J., Prabhu, D., Wright, M., Takashima, N., Hollis, B., and Sutton, K., "An Analysis of the Radiative Heating Environment for Aerocapture at Titan," AIAA Paper 2003-4953, July 2003.

[3] Wright, M. J., Bose, D., and Olejniczak, J., "Impact of Flowfield-Radiation Coupling on Aeroheating for Titan Aerocapture," *Journal of Thermophysics and Heat Transfer*, Vol. 19, No. 1, 2005, pp. 17–27.

[4] Olejniczak, J., Prabhu, D. K., Bose, D., and Wright, M. J., "Aeroheating Analysis for the Afterbody of a Titan Probe," AIAA Paper 2004-0486, Jan. 2004.

[5] Wright, M. J., Hollis, B. R., Bose, D., and Walpot, L., "Post Flight Aerothermal Analysis of Huygens Probe," ESA Paper WPP-263, 2005.

[6] Wright, M. J., Olejniczak, J., Walpot, L., Raynaud, E., Magin, T., Caillaut, L., and Hollis, B. R., "A Code Calibration Study for Huygens Entry Aeroheating," AIAA Paper 2006-0382, Jan. 2006.

[7] Walpot, L. M., Caillault, L., Molina, R. C., Laux, C. O., and Blanquaertk, T., "Convective and Radiative Heat Flux Prediction of Huygens Entry on Titan," *Journal of Thermophysics and Heat Transfer*, Vol. 20, No. 4, 2006, pp. 663–671. doi:10.2514/1.20901

[8] Magin, T. E., Caillault, L., Bourdon, A., and Laux, C. O., "Nonequilibrium Radiative Heat Flux Modeling for the Huygens Entry Probe," *Journal of Geophysical Research*, Vol. 111, No. E7, July 2006, Paper E07S12. doi:10.1029/2005JE002616

[9] Deepak Bose, Michael J. Wright, David W. Bogdanoff, George A. Raiche, and Gary A. Allen Jr., "Modeling and Experimental Assessment of CN Radiation Behind a Strong Shock Wave," *Journal of Thermophysics and Heat Transfer*, Vol. 20, No. 2, 2006, pp. 220–230; also AIAA Paper 2005-768, Jan. 2005.

[10] Kolesnikov, A. F., "Combined Measurements and Computations of High Enthalpy and Plasma Flows for Determination of TPM Surface Catalycity," Measurement Techniques for High Temperature and Plasma Flows, NATO RTO-EN-8, Apr. 2000, pp. 8A 1–16.

[11] Laux, C. O., "Optical Diagnostics and Radiative Emission of Air Plasma," High Temperature Gasdynamics Lab. Rept. T-288, Stanford Univ., Stanford, CA, Aug. 1993.

[12] Laux, C. O., "Radiation and Nonequilibrium Collisional Radiative Models," *Physico-Chemical Models for High Enthalpy and Plasma Flows*, Von Kármán Institute Lecture Series 2002–07, von Kármán Inst., Belgium, 2002.

[13] Playez, M., "Titan Atmosphere Plasma Investigation Using Spectroscopic Techniques," Ph.D. Dissertation, Von Kármán Inst.—Ecole Centrale Paris, Paris, June 2006.

[14] Park, C. S., Bershader, D., and Park, C., "Radiative Emission from the Simulated Shock Layer of Huygens Probe," *Journal of Thermophysics and Heat Transfer*, Vol. 10, No. 4, 1996, pp. 563–569.

[15] Labracherie, L., Billiotte, M., and Houas, L., "Shock-Tube Analysis of Argon Influence in Titan Radiative Environment," *Journal of Thermophysics and Heat Transfer*, Vol. 10, No. 1, 1996, pp. 162–168.

[16] Koffi-Kpante, K., Zeitoun, D., and Labracherie, L., "Computation and Experimental Validation of N_2-CH_4-Ar Mixture Flows Behind Normal

Shock Wave," *Shock Waves*, Vol. 7, No. 6, 1997, pp. 351–361. doi:10.1007/s001930050090

[17] Ramjaun, D., Dumitrescu, M., and Brun, R., "Kinetics of Free Radicals Behind Strong Shock Waves," *Journal of Thermophysics and Heat Transfer*, Vol. 13, No. 2, 1999, pp. 219–225.

[18] VandenAbeele, D., "An Efficient Computational Model for Inductively Coupled Air Plasma Flows Under Thermal and Chemical Non-equilibrium—With Application to Atmospheric Re-Entry Flow Studies," Ph.D. Dissertation, Katholieke Univ. Leuven/Von Kármán Inst., Belgium, 2000.

[19] Ito, H., Ozaki, Y., Suzuki, K., Kondow, T., and Kuchitsu, K., "Analysis of the $B^2\Sigma^+ \sim A^2\Pi_i$ Perturbations in the CN($B^2\Sigma^+$-$X^2\Sigma^+$) Main Band System," *Journal of Molecular Spectroscopy*, Vol. 127, No. 1, 1988, pp. 143–155. doi:10.1016/0022-2852(88)90015-X

[20] Peter J. Knowles, Werner, H.-J., Hay, P. J., and Cartwright, D. C., "The $A^2\Pi_i$-$X^2\Sigma^+$ and $B^2\Sigma^+$-$X^2\Sigma^+$ Violet Systems of the CN Radical: Accurate Multireference CI Calculations of the Radiative Transition Probabilities," *Journal of Chemical Physics*, Vol. 89, No. 12, 1988, pp. 7334–7343. doi:10.1063/1.455264

[21] Kuznetsova, L., and Stepanov, N., "Recommendations from the Raden Database for the Electronic Transition Moments on Diatomic Molecules of Astrophysical Interest, 1: C_2, CH and CN Molecules," *Astronomical and Astrophysical Transactions*, Vol. 12, No. 4, 1997, pp. 289–311. doi:10.1080/10556799708232084

[22] Prasad, C., and Bernath, P., "Fourier Transform Jet-Emission Spectroscopy of the $A^2\Pi_i$-$X^2\Sigma^+$ Transition of CN," *Journal of Molecular Spectroscopy*, Vol. 156, No. 2, 1992, pp. 327–340. doi:10.1016/0022-2852(92)90235-G

[23] Kotlar, A. J., Field, R. W., and Steinfeld, J. I., "Analysis of Perturbations in the $A^2\Pi$-$X^2\Sigma^+$ Red System of CN," *Journal of Molecular Spectroscopy*, Vol. 80, No. 1, 1980, pp. 86–108. doi:10.1016/0022-2852(80)90272-6

[24] Phillips, J. G., "Perturbations in the Swan System of the C_2 Molecule," *Journal of Molecular Spectroscopy*, Vol. 28, No. 2, 1968, pp. 233–242. doi:10.1016/0022-2852(68)90008-8

[25] Tanabashi, A., and Amano, T., "New Identification of the Visible Bands of the C_2 Swan System," *Journal of Molecular Spectroscopy*, Vol. 215, No. 2, October 2002, pp. 285–294. doi:10.1006/jmsp.2002.8645

[26] Arnold, J. O., and Langhoff, S. R., "Theoretical Study of the Electronic Transition Moment for the C_2 Swan Band System," *Journal of Quantitative Spectroscopy and Radiative Transfer*, Vol. 19, May 1978, pp. 461–466. doi:10.1016/0022-4073(78)90013-4

[27] Douay, M., Nietmann R., and, Bernath, P. F., "New Observations of the $A^1\Pi_u - X^1\Sigma_g^+$ Transition (Phillips System) of C_2," *Journal of Molecular Spectroscopy*, Vol. 131, No. 2, 1988, pp. 250–260. doi:10.1016/0022-2852(88)90236-6

[28] Chabalowski, C. F., and Peyerimhoff, S. D., "The Ballik-Ramsay, Mulliken, Deslandres-D'Azambuja and Phillips System in C_2: A Theoretical Study of Their Electronic Transition Moments," *Chemical Physics*, Vol. 81, Nos. 1–2, 1983, pp. 57–72. doi:10.1016/0301-0104(83)85302-6

[29] Martin, M., "C_2 Spectroscopy and Kinetics," *Journal of Photochemistry and Photobiology, A: Chemistry*, Vol. 66, No. 3, 1992, pp. 263–289. doi:10.1016/1010-6030(92)80001-C

[30] Roux, F., and Michaud, F., "High-Resolution Spectrometry of $^{14}N_2$ Infrared Emission Spectrum: Extensive Analysis of the $B^3\Pi_g$-$A^3\Sigma_u^+$ System," *Journal of Molecular Spectroscopy*, Vol. 97, No. 2, 1983, pp. 253–265. doi:10.1016/0022-2852(83)90266-7

[31] Roux, F., and Michaud, F., "Investigation of the Rovibrational Levels of the $B^3\Pi_g$ state of $^{14}N_2$ Molecule Above the Dissociation Limit $N(^4S) + N(^4S)$ by Fourier Transform Spectrometry," *Canadian Journal of Physics*, Vol. 68, No. 11, 1990, pp. 1257–1261.

[32] Roux, F., and Michaud, F., "High-Resolution Fourier Spectrometry of $^{14}N_2$ Violet Emission Spectrum: Extensive Analysis of the $C^3\Pi_u \rightarrow B^3\Pi_g$ System," *Journal of Molecular Spectroscopy*, Vol. 158, No. 2, 1993, pp. 270–277. doi:10.1006/jmsp.1993.1071